JACS
JOURNAL OF THE AMERICAN CHEMICAL SOCIETY
Communication
pubs.acs.org/JACS

High Curie Temperature $Bi_{1.85}Mn_{0.15}Te_3$ Nanoplates

Lina Cheng,[†] Zhi-Gang Chen,*[,†] Song Ma,[‡] Zhi-dong Zhang,[‡] Yong Wang,[†] Hong-Yi Xu,[†] Lei Yang,[†] Guang Han,[†] Kevin Jack,[§] Gaoqing (Max) Lu,[⊥] and Jin Zou*[,†,§]

[†]Materials Engineering, [§]Centre for Microscopy and Microanalysis, and [⊥]ARC Centre of Excellence for Functional Nanomaterials, Australian Institute for Bioengineering and Nanotechnology, The University of Queensland, St Lucia, QLD 4072, Australia

[‡]Shenyang National Laboratory of Material Sciences, Institute of Metal Research, Chinese Academy of Sciences, Shenyang 110016, P.R. China

Supporting Information

ABSTRACT: $Bi_{1.85}Mn_{0.15}Te_3$ hexagonal nanoplates with a width of ~200 nm and a thickness of ~20 nm were synthesized using a solvothermal method. According to the structural characterization and compositional analysis, the Mn^{2+} and Mn^{3+} ions were found to substitute Bi^{3+} ions in the lattice. High-level Mn doping induces significant lattice distortion and decreases the crystal lattice by 1.07% in the *a* axis and 3.18% in the *c* axis. A high ferromagnetic state with a Curie temperature of ~45 K is observed in these nanoplates due to Mn^{2+} and Mn^{3+} ion doping, which is a significant progress in the field of electronics and spintronics.

Bi_2Te_3 is a well-known candidate for applications as a thermoelectric material or topological insulator, and it has been confirmed to have a conducting surface state with a single non-degenerate Dirac cone with linear dispersion in the momentum space.[1−7] With the eye-catching development of topological insulators on both the theoretical and experimental fronts, research referring to the profound aspect of modern physics, such as quantized anomalous Hall effect[8−11] and topological magnetoelectric effect,[12−14] is triggered. Meanwhile, breaking the time reversal symmetry caused by the introduction of magnetic impurities into these materials can induce a gap at the Dirac point of the topological surface state, which is crucial for the realization of the exotic phenomena mentioned above.[15−19] Therefore, the coexistence of both magnetic order and topological state in these topological-based materials, especially on the nanoscale, is exciting for the future development of nano-spintronic devices.

To date, significant effort has been devoted to developing long-range magnetic ordered Bi_2Te_3 in topological insulators by doping with transition metals.[20−23] Very recently, experiments have shown that substitution of transition metals into Bi_2Te_3 can tune the electrical and magnetic properties of Bi_2Te_3 systems.[24] Many transition metals, such as Fe,[15,25−27] Cr,[28−30] Mn,[20,21,24,31] V,[32] and Sn,[33] are substituted into bulk Bi_2Te_3 to produce dilute magnetic topological semiconductors. For example, for bulk Bi_2Te_3, ferromagnetic ordering at the Curie temperature (T_c = 10 K) was reported for Mn^{2+} substitution of Bi^{3+}.[31] Current research has focused on bulk Bi_2Te_3 materials doped with transition metals by various methods, such as the Bridgman,[34] vertical gradient solidification,[31] and vapor−liquid−solid methods.[27] On the other hand, magnetic impurities doped into the Bi_2Te_3 nanostructures are rarely reported. It should be noted that, when compared with the traditional bulk topological insulators, nanomaterials not only reveal more enhanced and novel physical properties[35−37] but are also leading the way as devices for future spintronics industries. For example, for bulk Bi_2Te_3 materials, the direct manipulation of their edge/surface states is relatively difficult to achieve because they are significantly outnumbered by the bulk carriers.[38−42] In contrast, our previous efforts have achieved enhanced surface conduction by manipulating the surface states in Bi_2Te_3 nanoribbons[38] and Bi_2Te_3 nanoplates[43] synthesized by a solvothermal method. It is anticipated that the doping of magnetic impurities into such Bi_2Te_3 nanostructures would lead to a gap at the Dirac point of the topological surface state, which may also move progress in spintronics ahead by leaps and bounds.

In this study, we demonstrate that magnetic Mn^{2+} and Mn^{3+} can be readily doped into Bi_2Te_3 hexagonal nanoplates by a low-cost and controllable solvothermal method. Through detailed structural and compositional characterizations, Mn^{2+} and Mn^{3+} are found to substitute Bi^{3+} ions, which not only leads to a decrease of the lattice parameters in the Bi_2Te_3 crystal structure but also causes ferromagnetic ordering at a relevantly high T_c = 45 K. This transition temperature is higher than that of bulk materials.

Figure 1a shows typical high-sensitivity X-ray diffraction (XRD) patterns, collected with synchrotron radiation, of the as-prepared doped and undoped samples (detailed synthesis procedure is given in the Supporting Information). The XRD pattern of the Mn-doped sample can be indexed exclusively as Bi_2Te_3 with a rhombohedral structure, and all diffraction peaks shift toward lower diffraction angles (this can be seen by comparing with the XRD pattern of undoped Bi_2Te_3). The shift in diffraction peaks might be caused by the Mn doping. More importantly, the fact that no other diffraction peaks were observed indicates that the products are of high purity. The lattice parameters of the Mn-doped Bi_2Te_3 are determined to be *a* = 4.35 Å and *c* = 29.51 Å, decreases of 1.07% in the *a* axis and 3.18% in the *c* axis when compared with those of undoped Bi_2Te_3 (see Table S1). Figure 1b shows a representative low-magnification scanning electron microscopy (SEM) image of

Received: September 8, 2012
Published: November 5, 2012

   dx.doi.org/10.1021/ja308933k | J. Am. Chem. Soc. 2012, 134, 18920−18923

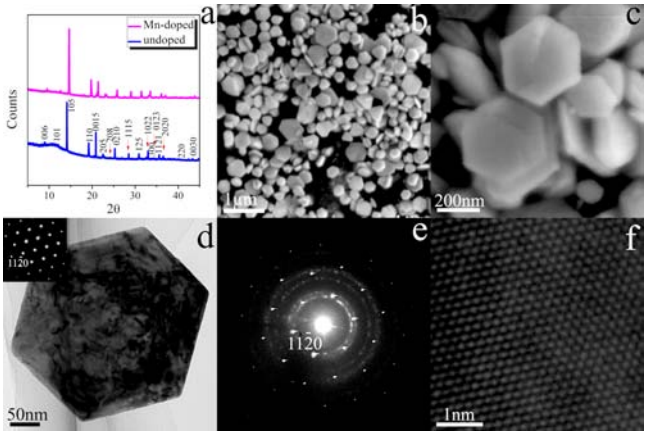

Figure 1. Structural characteristics of as-prepared doped and undoped samples: (a) synchrotron radiation XRD patterns; (b) low-magnification SEM image; (c) high-magnification SEM image; (d) TEM image for a typical nanoplate; (e) SAED pattern taken from the Pt-coated TEM sample; (f) high-resolution TEM image for the nanoplate in (d).

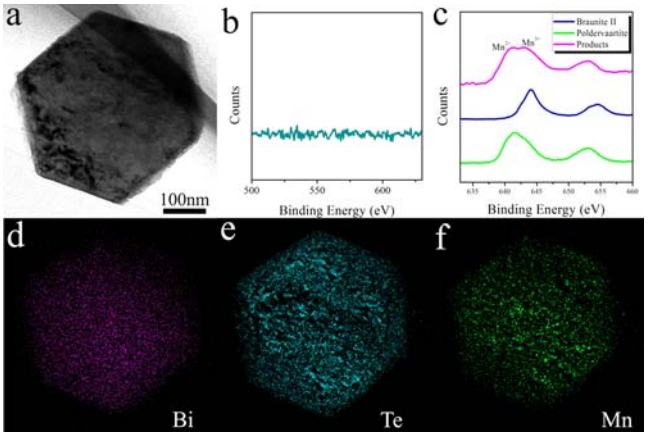

Figure 2. Compositional analyses of the as-prepared products: (a) bright-field TEM image for a typical nanoplate; (b) EELS spectrum taken near the O edge, showing no O existence; (c) EELS spectra of the Mn edge of the nanoplate and Mn-L2,3-edges taken from standard Mn^{2+} and Mn^{3+} manganese oxides; (d–f) EELS mapping of Bi, Te, and Mn.

the as-prepared products, in which nanoplates can be clearly observed. From the high-magnification SEM image (Figure 1c), the nanoplates are observed to have hexagonal facets with lateral dimension of ~200 nm and a thickness of ~20 nm (see the SEM and transmission electron microscopy (TEM) images and thickness distribution data in Figure S1). To understand the structural characteristics of such hexagonal nanoplates, further detailed TEM characterizations were carried out. The bright-field TEM image in Figure 1d demonstrates such a hexagonal nanoplate. The corresponding selected area electron diffraction (SAED) pattern (inset of Figure 1d) indicates that the surface normal of the hexagonal nanoplate is parallel to the *c* axis. The six side edges can be determined to be $\{10\bar{1}0\}$ facets. To accurately determine the lattice spacings of our products, the TEM specimens were coated with Pt nanoparticles with well-defined lattice spacings. Figure 1e shows a SAED pattern superimposed with diffraction rings raised from Pt nanoparticles. Using Pt diffraction rings as a reference (a_{Pt} = 3.925 Å), $d\{11\bar{2}0\}$ = 2.17 Å can be determined, which is in excellent agreement with the results determined from the synchrotron XRD. A typical high-resolution TEM image is shown in Figure 1f, confirming that this product is highly crystalline.

To clarify the fundamental reason behind the decreased lattice spacing, chemical analysis, including electron dispersive spectroscopy and electron energy loss spectroscopy (EELS), was employed to determine the elemental speciation and distribution within the hexagonal nanoplates. Figure 2a shows a typical bright-field TEM image of a hexagonal nanoplate. Figure 2b,c shows EELS spectra taken from the nanoplate, in which no O EELS edge (should be at ~529 eV) is observed but the Mn-L2,3-edges at 640 and 650 eV are found, which can be indexed as Mn^{2+} and Mn^{3+} (standard Mn-L2,3-edges from Mn^{2+} and Mn^{3+} manganese oxides as reference data[44] are shown in Figure 2c). Therefore, two doped states of Mn (Mn^{2+} and Mn^{3+}) are observed to co-exist in the nanoplates. To further clarify the distribution of the elements Bi, Te, and Mn, EELS maps were collected and are shown in Figure 2d–f, respectively. From the contrast of Figure 2f, Mn can be identified to be uniformly distributed within the nanoplates. Due to the different doped states of Mn (Mn^{2+} and Mn^{3+}), additional X-ray photoelectron spectroscopy (XPS) was performed to determine the bonding behavior of our products. Figure 3 shows such an XPS spectrum, with the insets being those of the enlarged spectra

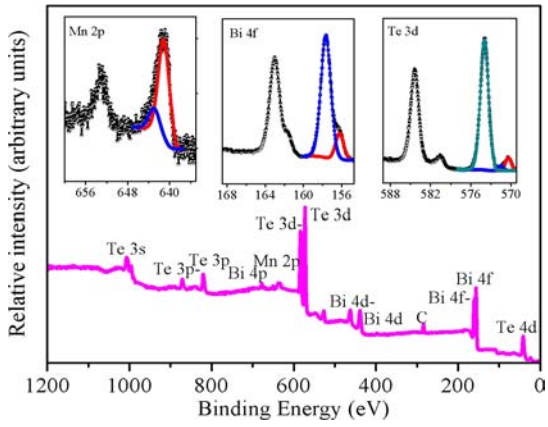

Figure 3. XPS analysis for the as-prepared nanoplates and enlarged spectra of Mn 2p, Bi 4f, and Te 3d.

(i.e., high-resolution narrow scans) for selected individual elements. The predominant measured binding energies for Bi and Te, corresponding to the Bi_2Te_3 phase, are 157.8 eV for Bi and 573.7 eV for Te, respectively.[45,46] Note also that, for each of the narrow scans shown in Figure 3, the XPS spectra show two series of peaks which are separated by a defined energy and are in a defined ratio (e.g, 2:1, 3:2, and 4:3 for the 2p, 3d, and 4f orbitals, respectively) due to spin–orbit coupling. The discussion to follow, therefore, focuses on the most intense peaks at the lower binding energy. In the narrow scan of the Bi 4f region, a shoulder at ~156.6 eV is observed on the main peak at 157.8 eV, which is different from the reported Bi–O binding energy at 158.5–161.5 eV.[47] Therefore, we attribute this binding energy to the Bi atoms in the vicinity of the Mn dopants. As can also be seen, two bonding states are observed in the Te 3d region at binding energies of 572.2 and 571.5 eV, which are significantly different than expected for a Te–O binding energy of 576.0–577.5 eV.[47] In addition, there is little evidence for oxygen in the XPS spectrum. Therefore, two kinds of Mn–Te bonds are believed to coexist in our sample, ascribed

dx.doi.org/10.1021/ja308933k | J. Am. Chem. Soc. 2012, 134, 18920–18923

to those between Te and Mn^{2+} and Mn^{3+} which were observed in the EELS measurements shown in Figure 2c. Through quantitative analysis of the XPS spectra, the composition of the elements Bi, Te, and Mn was calculated as ~37.1%, 59.9%, and 3.0%, respectively, which is equivalent to a Bi:Te:Mn ratio of 12.4:20.0:1.0. Therefore, the composition of the sample is defined as $Bi_{1.85}Mn_{0.15}Te_3$, in which the Mn atoms have substituted at the position of the Bi atoms. In fact, the ionic radii and covalent radii of Mn are smaller than those of Bi, so substituting Mn atoms for Bi atoms should lead to decreased lattice parameters of the synthesized products, which is consistent with the obtained XRD results.

Based on the detailed structural, chemical, and bonding characterizations outlined above, we have achieved Mn-doped Bi_2Te_3 with Mn replacing Bi. For such a compound, magnetic properties are expected. A SQUID magnetometer was used to examine temperature-dependent magnetization in zero-field cooled (ZFC) and field-cooled (FC) processes; the magnetic field dependence of the magnetization and hysteresis loops at 5 K is shown in Figure 4. The ZFC curve was obtained by cooling

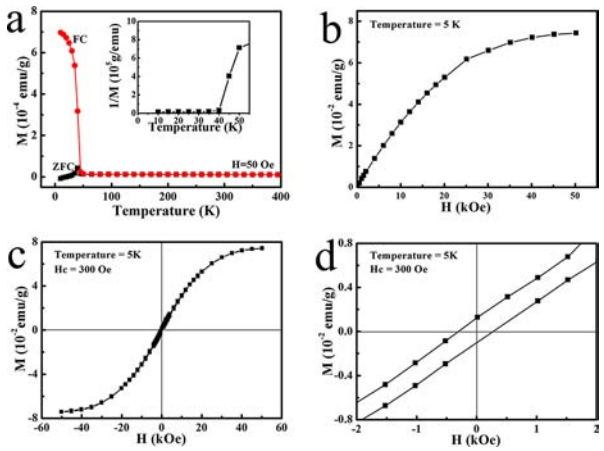

Figure 4. Magnetic properties of the $Bi_{1.85}Mn_{0.15}Te_3$ nanoplates: (a) temperature-dependent magnetization moments in ZFC and FC processes under the measuring field of 50 Oe; (b) $M-H$ profile at 5 K; (c) hysteresis loops at 5 K; (d) enlarged central section of (c).

the sample in the absence of a magnetic field from 400 to 10 K, and subsequently measuring the magnetic moments while the sample was warmed under a field of 50 Oe. For the FC process, however, the sample is cooled through its Curie temperature in the presence of a magnetic field (50 Oe). The difference between these two processes provides important insight into the phase transition temperature (T_C) and blocking temperature (T_B). Based on the temperature-dependent ZFC and FC curves and hysteresis loops shown in Figure 4, the $Bi_{1.85}Mn_{0.15}Te_3$ nanoplates show several features, as elaborated in the following: (a) The ZFC and FC curves have a turning point at ~45 K, indicating that the $Bi_{1.85}Mn_{0.15}Te_3$ nanoplates have a magnetic transition at ~45 K. (b) The existing peak at the ZFC curve indicates the T_B (30 K) of the $Bi_{1.85}Mn_{0.15}Te_3$ nanoplates. (c) The $M-H$ curve demonstrates the typical ferromagnetic behavior of $Bi_{1.85}Mn_{0.15}Te_3$ nanoplates at T = 5 K, from which the saturation magnetization can be determined as 0.074 emu/g. As mentioned above, Mn ions are doped in the nanoplates. Therefore, the magnetic moments originate from the doped Mn ions, and the ferromagnetic behavior is contributed by the spin polarization of the electric band structure of $Bi_{1.85}Mn_{0.15}Te_3$, which is similar to the experimental results for bulk crystalline $Bi_{1.91}Mn_{0.09}Te_3$.[34] However, the higher Curie temperature, at ~45 K, for the $Bi_{1.85}Mn_{0.15}Te_3$ nanoplates as compared to that of bulk $Bi_{1.91}Mn_{0.09}Te_3$, at 12 K, indicates that the increasing content of doped Mn ions (tuning the carriers density[34,48]) or quantum confinement of carriers[49] in such thin $Bi_{1.85}Mn_{0.15}Te_3$ nanoplates (~20 nm) may lead to the enhancement of the Curie temperature for the topological phase Bi_2Te_3. (d) Hysteresis loop with H_c = 300 Oe at 5 K shows the typical soft magnetic performance, expected with the observed ferromagnetic performance. This achievement of forming magnetic $Bi_{1.85}Mn_{0.15}Te_3$ nanoplates represents significant progress in the field of electronics and spintronics.

In conclusion, uniform $Bi_{1.85}Mn_{0.15}Te_3$ hexagonal nanoplates were successfully synthesized by the solvothermal method. Based on the structural, chemical, and bonding characteristics, the substitution of smaller Mn^{2+} and Mn^{3+} ions for the Bi^{3+} ions in the crystal lattice leads to reduced lattice parameters. Doping the magnetic element Mn in the Bi_2Te_3 nanoplates caused the transition to a ferromagnetic state at T_c = 45 K. This study paves the way to develop tunable magnetic nanostructures (Figures S2 and S3) for the design and development of future electronic and spintronic devices.

■ ASSOCIATED CONTENT

Supporting Information

Synthesis procedure, determination of *d* spacing, determination of thickness of the $Bi_{1.85}Mn_{0.15}Te_3$ hexagonal nanoplates and its distribution, Raman spectra of undoped and Mn-doped Bi_2Te_3 nanoplates, and Mn 2p XPS spectra of various Mn-doped Bi_2Te_3 nanoplates. This material is available free of charge via the Internet at http://pubs.acs.org.

■ AUTHOR INFORMATION

Corresponding Author

j.zou@uq.edu.au; z.chen1@uq.edu.au

Notes

The authors declare no competing financial interest.

■ ACKNOWLEDGMENTS

This work was supported by the Australian Research Council. Z.-G.C. thanks the QLD government for a smart state future fellowship and a UQ research foundation excellent award. This work was also supported by the National Natural Science Foundation of China (50901078) and the National High Technology Research and Development Program of China (2011AA03A402). The authors acknowledge the facilities, and the scientific and technical assistance, of the Australian Microscopy & Microanalysis Research Facility at the Centre for Microscopy and Microanalysis, The University of Queensland. In addition, this work was carried out in part on the Powder Diffraction Beamline at the Australian Synchrotron, Clayton, Victoria.

■ REFERENCES

(1) Chen, Y. L.; Analytis, J. G.; Chu, J. H.; Liu, Z. K.; Mo, S. K.; Qi, X. L.; Zhang, H. J.; Lu, D. H.; Dai, X.; Fang, Z.; Zhang, S. C.; Fisher, I. R.; Hussain, Z.; Shen, Z. X. *Science* **2009**, *325*, 178.

(2) Zhang, T.; Cheng, P.; Chen, X.; Jia, J.-F.; Ma, X.; He, K.; Wang, L.; Zhang, H.; Dai, X.; Fang, Z.; Xie, X.; Xue, Q.-K. *Phys. Rev. Lett.* **2009**, *103*, 266803.

(3) Zhang, H.; Liu, C.-X.; Qi, X.-L.; Dai, X.; Fang, Z.; Zhang, S.-C. *Nature Phys.* **2009**, *5*, 438.

(4) Teweldebrhan, D.; Goyal, V.; Balandin, A. A. *Nano Lett.* **2010**, *10*, 1209.
(5) Goyal, V.; Teweldebrhan, D.; Balandin, A. A. *Appl. Phys. Lett.* **2010**, *97*, 133117.
(6) Shahil, K. M. F.; Hossain, M. Z.; Teweldebrhan, D.; Balandin, A. A. *Appl. Phys. Lett.* **2010**, *96*, 153103.
(7) Li, H.; Cao, J.; Zheng, W. S.; Chen, Y. L.; Wu, D.; Dang, W. H.; Wang, K.; Peng, H. L.; Liu, Z. F. *J. Am. Chem. Soc.* **2012**, *134*, 6132.
(8) Qu, D.-X.; Hor, Y. S.; Xiong, J.; Cava, R. J.; Ong, N. P. *Science* **2010**, *329*, 821.
(9) Zitko, R. *Phys. Rev. B* **2010**, *81*, 241414.
(10) Jiang, H.; Qiao, Z.; Liu, H.; Niu, Q. *Phys. Rev. B* **2012**, *85*, 045445.
(11) Yu, R.; Zhang, W.; Zhang, H.-J.; Zhang, S.-C.; Dai, X.; Fang, Z. *Science* **2010**, *329*, 61.
(12) Cheng, F. *Solid State Commun.* **2012**, *152*, 933.
(13) Kulbachinskii, V. A.; Gurin, P. V.; Tarasov, P. M.; Davydov, A. B.; Danilov, Y. A.; Vikhrova, O. V. *Low Temp. Phys.* **2007**, *33*, 174.
(14) Mondal, S.; Sen, D.; Sengupta, K.; Shankar, R. *Phys. Rev. B* **2010**, *82*, 045120.
(15) Rosenberg, G.; Franz, M. *Phys. Rev. B* **2012**, *85*, 195119.
(16) Fu, Z.-G.; Zhang, P.; Wang, Z.; Li, S.-S. *J. Phys.-Condes. Matter* **2012**, *24*, 145502.
(17) Habe, T.; Asano, Y. *Phys. Rev. B* **2012**, *85*, 195325.
(18) Foster, M. S. *Phys. Rev. B* **2012**, *85*, 085122.
(19) Chen, Y. L.; Chu, J. H.; Analytis, J. G.; Liu, Z. K.; Igarashi, K.; Kuo, H. H.; Qi, X. L.; Mo, S. K.; Moore, R. G.; Lu, D. H.; Hashimoto, M.; Sasagawa, T.; Zhang, S. C.; Fisher, I. R.; Hussain, Z.; Shen, Z. X. *Science* **2010**, *329*, 659.
(20) Bos, J. W. G.; Lee, M.; Morosan, E.; Zandbergen, H. W.; Lee, W. L.; Ong, N. P.; Cava, R. J. *Phys. Rev. B* **2006**, *74*, 184429.
(21) Choi, J.; Choi, S.; Park, Y.; Park, H. M.; Lee, H. W.; Woo, B. C.; Cho, S. *Phys. Status Solidi B* **2004**, *241*, 1541.
(22) Thalmeier, P. *Phys. Rev. B* **2011**, *84*, 155102.
(23) Men'shov, V. N.; Tugushev, V. V.; Chulkov, E. V. *JETP Lett.* **2011**, *94*, 629.
(24) Niu, C.; Dai, Y.; Guo, M.; Wei, W.; Ma, Y.; Huang, B. *Appl. Phys. Lett.* **2011**, *98*, 252502.
(25) Kulbachinskii, V. A.; Kaminskii, A. Y.; Kindo, K.; Narumi, Y.; Suga, K.; Lostak, P.; Svanda, P. *Physica B* **2002**, *311*, 292.
(26) West, D.; Sun, Y. Y.; Zhang, S. B.; Zhang, T.; Ma, X.; Cheng, P.; Zhang, Y. Y.; Chen, X.; Jia, J. F.; Xue, Q. K. *Phys. Rev. B* **2012**, *85*, 081305.
(27) Cha, J. J.; Williams, J. R.; Kong, D.; Meister, S.; Peng, H.; Bestwick, A. J.; Gallagher, P.; Goldhaber-Gordon, D.; Cui, Y. *Nano Lett.* **2010**, *10*, 1076.
(28) Kulbachinskii, V. A.; Tarasov, P. M.; Bruck, E. *Physica B* **2005**, *368*, 32.
(29) Kulbachinskii, V. A.; Tarasov, P. M.; Bruck, E. *J. Exp. Theor. Phys.* **2005**, *101*, 528.
(30) Haazen, P. P. J.; Laloe, J. B.; Nummy, T. J.; Swagten, H. J. M.; Jarillo-Herrero, P.; Heiman, D.; Moodera, J. S. *Appl. Phys. Lett.* **2012**, *100*, 082404.
(31) Choi, J.; Lee, H. W.; Kim, B. S.; Choi, S.; Song, J. H.; Cho, S. L. *J. Appl. Phys.* **2005**, *97*, 10D324.
(32) Dyck, J. S.; Hajek, P.; Losit'ak, P.; Uher, C. *Phys. Rev. B* **2002**, *65*, 115212.
(33) Zhang, H. B.; Yu, H. L.; Bao, D. H.; Li, S. W.; Wang, C. X.; Yang, G. W. *Adv. Mater.* **2012**, *24*, 132.
(34) Hor, Y. S.; Roushan, P.; Beidenkopf, H.; Seo, J.; Qu, D.; Checkelsky, J. G.; Wray, L. A.; Hsieh, D.; Xia, Y.; Xu, S. Y.; Qian, D.; Hasan, M. Z.; Ong, N. P.; Yazdani, A.; Cava, R. J. *Phys. Rev. B* **2010**, *81*, 195203.
(35) Peng, H.; Lai, K.; Kong, D.; Meister, S.; Chen, Y.; Qi, X.-L.; Zhang, S.-C.; Shen, Z.-X.; Cui, Y. *Nat. Mater.* **2010**, *9*, 225.
(36) Dang, W.; Peng, H.; Li, H.; Wang, P.; Liu, Z. *Nano Lett.* **2010**, *10*, 2870.
(37) Peng, H.; Dang, W.; Cao, J.; Chen, Y.; Wu, D.; Zheng, W.; Li, H.; Shen, Z.-X.; Liu, Z. *Nature Chem.* **2012**, *4*, 281.
(38) Xiu, F.; He, L.; Wang, Y.; Cheng, L.; Chang, L.-T.; Lang, M.; Huang, G.; Kou, X.; Zhou, Y.; Jiang, X.; Chen, Z.; Zou, J.; Shailos, A.; Wang, K. L. *Nat. Nanotechnol.* **2011**, *6*, 216.
(39) Fu, L.; Kane, C. L.; Mele, E. J. *Phys. Rev. Lett.* **2007**, *98*, 106803.
(40) Brumfiel, G. *Nature* **2010**, *466*, 310.
(41) Franz, M. *Nat. Mater.* **2010**, *9*, 536.
(42) Moore, J. *Nature Phys.* **2009**, *5*, 378.
(43) Wang, Y.; Xiu, F.; Cheng, L.; He, L.; Lang, M.; Tang, J.; Kou, X.; Yu, X.; Jiang, X.; Chen, Z.; Zou, J.; Wang, K. L. *Nano Lett.* **2012**, *12*, 1170.
(44) Calvert, C. C.; Gutzmer, J.; Banks, D. A.; Rainforth, W. M. *EMAG: Electron Microsc. Anal. Group Conf 2007* **2008**, *126*, 012045.
(45) Menke, E. J.; Brown, M. A.; Li, Q.; Hemminger, J. C.; Penner, R. M. *Langmuir* **2006**, *22*, 10564.
(46) Bando, H.; Koizumi, K.; Oikawa, Y.; Daikohara, K.; Kulbachinskii, V. A.; Ozaki, H. *J. Phys.-Condes. Matter* **2000**, *12*, 5607.
(47) Wagner, C. D.; Naumkin, A. V.; Kraut-Vass, A.; Allison, J. W. ; Powell, C. J. ; Rumble, J. R. , Jr. *NIST X-ray Photoelectron Spectroscopy Database*; NIST Standard Reference Database 20, Version 3.3; National Institute of Standards and Technology: Gaithersburg, MD, 2003; http://srdata.nist.gov/xps.
(48) Story, T.; Gałazka, R. R.; Frankel, R. B.; Wolff, P. A. *Phys. Rev. Lett.* **1986**, *56*, 777.
(49) Dietl, T.; Haury, A.; Merle d'Aubigné, Y. *Phys. Rev. B* **1997**, *55*, R3347.